IEEE Access
Multidisciplinary | Rapid Review | Open Access Journal

Received 19 October 2023, accepted 9 November 2023, date of publication 16 November 2023,
date of current version 22 November 2023.

Digital Object Identifier 10.1109/ACCESS.2023.3333869

RESEARCH ARTICLE

Dynamic Metasurface Reflectors Based on Coupled Resonators for Simultaneous Magnitude and Phase Control

MOHAMED K. EMARA[1], (Member, IEEE), DEBIDAS KUNDU[2], (Member, IEEE), KEIGAN MACDONELL[1], (Member, IEEE), LEANDRO M. RUFAIL[1], AND SHULABH GUPTA[1], (Senior Member, IEEE)

[1]Department of Electronics, Carleton University, Ottawa, ON K1S 5B6, Canada
[2]Department of Electronics and Communication Engineering, Indraprastha Institute of Information Technology, Delhi, New Delhi 110020, India

Corresponding author: Mohamed K. Emara (mohamedemara@cmail.carleton.ca)

This work was supported by the Department of National Defence's Innovation for Defence Excellence and Security (IDEaS) Program.

ABSTRACT A novel metasurface reflector unit cell based on two coupled resonators is proposed and demonstrated for real-time reconfigurable beamforming in the X-band (8-12 GHz). The unit cell is composed of a split-ring resonator (SRR) with tunable capacitance and a dipole-ring resonator (DRR) with tunable resistance, whose collective variations allow for control over the complex reflectance at a desired frequency. To gain physical insight into its working mechanism, the proposed unit cell is modeled as a coupled Lorentz oscillator using the surface susceptibility description of the unit cell. Thereafter, a metasurface reflector based on the proposed unit cell is demonstrated in full-wave simulations to achieve various beamforming examples, such as beam-steering, side-lobe level control, beam-steering with amplitude control, and multi-beam patterns, from a single normally-incident plane wave excitation. Three metasurface reflectors are fabricated to experimentally demonstrate the proposed concept; the first is based on an SRR with a varactor diode, the second is based on a DRR with a PIN diode, and the third is based on the proposed coupled SRR-DRR configuration with both varactor and PIN diodes, for simultaneous magnitude and phase control. The metasurface reflector based on the coupled resonator unit cell is experimentally demonstrated to achieve versatile beam transformations including beam-steering with amplitude control and multi-beam patterns.

INDEX TERMS Metasurface reflectors, beamforming, side-lobe level control, beam-steering, multi-beam patterns, complex reflectance, reconfigurable intelligent surfaces, coupled resonators, smart radio environments.

I. INTRODUCTION

Metasurfaces have emerged as practical tools for manipulating electromagnetic (EM) waves through the engineering of two-dimensional sub-wavelength scatterers. They have been proposed across the frequency spectrum for various functionalities such as anomalous refraction and reflection [1], [2], [3], absorption [4], [5], [6], polarization conversion [7], [8], [9], and cloaking [10], [11], [12], to name a few. An important application of metasurfaces has been found in wireless communication, specifically for developing smart radio environments [13]. Future networks will be required to meet the ever-increasing demand for seamless connectivity with higher capacity, data rates, and reliablilty and lower latency [14], [15]. Reconfigurable intelligent surfaces (RIS) have been conceptualized as one of the most attractive and cost-effective means of EM wave control in wireless environments [16], [17]. Reconfigurable metasurface reflectors are a practical implementation whose tunable complex reflectance allows for real-time beamforming in the far-field.

Far-field beamforming can be achieved by controlling the complex weights of the reflected field over the metasurface aperture. Magnitude control allows for beamforming such as side-lobe level (SLL) control through aperture

The associate editor coordinating the review of this manuscript and approving it for publication was Davide Ramaccia.

field amplitude tapering, binary amplitude grating [18] to generate multi-beam patterns, and reflected power control. Phase control allows for beamforming such as beam-steering through engineered phase gradients, binary phase grating [18] to generate multi-beam patterns, and beam focusing. Therefore, a full and simultaneous magnitude-phase control is a necessity to allow for rich beamforming capabilities such as generating asymmetrical multi-beam patterns with different gains.

To meet the goal of achieving extensive beamforming capabilities, numerous metasurface designs have been proposed for realizing both magnitude and phase control. For instance, a metasurface reflector was proposed in [19] for arbitrary magnitude and phase control based on spatial rotation of X-shaped rectangular metal rods. However, the design is limited to static implementations without a clear path for reconfigurability. Moreover, this technique, based on the Pancharatnam-Berry phase effect [20], [21], inherently produces unwanted cross-polarized reflection. Another example is a static metasurface reflector based on coupled resonators which was proposed in [22]. The design consists of resonators coupled across multiple dielectric layers and provides excellent control over complex reflectance via dimensional changes of the resonators. Similarly, a passive and lossless metasurface reflector based on surface waves was recently proposed in [23] and demonstrated for dual-beam reflection with simultaneous control of each beam's direction and power. However, both these designs are not easily scalable for dynamic variation of complex reflectance.

To achieve reconfigurable magnitude and phase control, active components, such as PIN and varactor diodes [24], and graphene [25], to name a few, are mainly used. A reconfigurable metasurface reflector based on two varactor diodes was recently proposed in [26] with a demonstration of simultaneous and independent magnitude and phase control for single-plane beamforming. The reconfigurable unit cell design is based on DC bias lines connecting adjacent unit cells along one direction. The DC bias lines are also exposed to incoming radiation, and therefore force the operating polarization to be linear only. Moreover, its evolution to a cell-by-cell active control is not readily possible due this same reason. As a result, unit cells sharing bias lines exhibit the same electrical properties, hence the beamforming is inherently limited to a single plane perpendicular to the bias lines. Another reconfigurable metasurface reflector with magnitude and phase control was proposed in [27]. It is based on two individual modules, one for controlling the magnitude and the other for the phase, with the modules separated by an air gap. Similar to [26], the biasing is achieved on a column-by-column basis and hence beamforming is limited to a single plane. Moroever, this configuration is not low-profile.

Mechanical control has also been explored as means of designing reconfigurable metasurfaces. For instance, an electro-mechanical reconfigurable metasurface reflector was proposed in [28], where phase control is achieved through a motorized vertical displacement of the unit cell and magnitude is controlled through a PIN diode integrated in a split-ring resonator (SRR). While the design presents de-coupled control over magnitude and phase control, it suffers from slow reconfiguration speed, heavy weight, bulkiness, and high power consumption of the motors. There are other implementations of mechanically reconfigurable metasurface available but they provide only phase control [29], [30].

Joint magnitude and phase control has also been attempted in coding metasurface-based reflectors. In [31], a unit cell is proposed which jointly exhibits 1-bit phase and multi-bit magnitude coding using a PIN diode. A PIN diode is attractive due to its low-loss characteristics compared to a varactor diode which typically is not only lossy, but also relatively more expensive. In [32], a meta-atom embedded with a PIN diode and a resistor is proposed to achieve 1-bit phase coding for y-polarized incidence and 1-bit magnitude coding for x-polarized incidence. However, these coding metasurface reflectors with few quantized phase and magnitude states, instead of continuous phase and magnitude tunability, show limitations in attaining arbitrary beamforming. Furthermore, coding metasurfaces have limited beamforming capability under far-field wave excitation as opposed to dedicated near-field sources.

An ideal metasurface reflector should offer continuous magnitude and phase tunability, be scalable to cell-by-cell control, be capable of handling multiple polarizations, feature low-profile, and include as low a number of external circuit elements as possible in order to lower losses and cost. To address some of these requirements, in [33], the authors proposed a unit cell concept based on two coupled resonators with three controls (two capacitive and one resistive) for enhanced control over the complex reflectance, and demonstrated the performance for static beamforming using capacitors and resistors. While a dynamic version of this unit cell using varactor and PIN diodes is theoretically attainable, it will involve a complex DC biasing architecture in addition to RF-DC isolation considerations at each component. Moreover, it will increase prototyping and assembly costs considering that a typical metasurface requires hundreds of these lumped components, owing to the electrically large surface areas.

To overcome this complexity while maintaining the advantages of the coupled resonator configuration, a simplified version of a coupled-resonator-based unit cell with two controls is proposed here. Similar to [33], the new unit cell is based on two coupled resonators; an SRR and a DRR. However in the new configuration, the SRR has a tunable capacitance and a tunable resistance that is integrated inside the DRR. This configuration uses fewer components (i.e., a varactor and a PIN diode only) and features a simpler DC biasing mechanism based on printed radial-line stubs, at the cost of compromised complex reflectance coverage

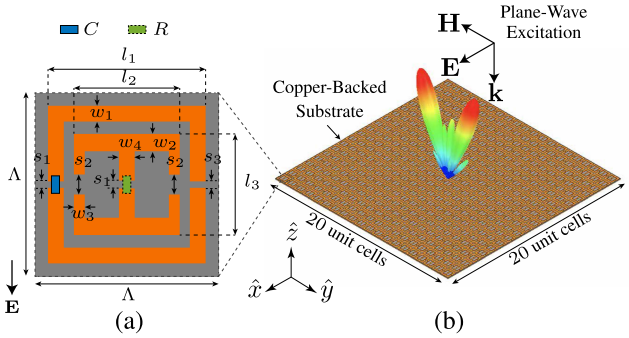

FIGURE 1. (a) Illustration of the proposed unit cell based on an SRR with tunable capacitance (e.g., using a varactor diode) and a DRR with tunable resistance (e.g., using a PIN diode). (b) Demonstration of the unit cell in a 20 × 20–unit cell array to generate a dual-beam pattern from a normally-incident plane wave.

compared to a near-ideal configuration of [33]. Nonetheless the unit cell can achieve versatile beam transformations as will be demonstrated. The unit cell is fully RF-DC isolated and is designed with the biasing network placed behind the ground plane for minimal interaction with the incoming radiation. This allows the unit cells to be physically isolated from each other, paving a clear path for cell-by-cell control.

The rest of the paper is organized as follows. Sec. II presents the evolution of the proposed unit cell starting from a single resonator that leads to various configurations of coupled resonators. Sec. III presents theoretical analysis of the unit cell response via a coupled Lorentz oscillator model representing a simple way to model the unit cell, while providing further insights into its operation. Sec. IV presents full-wave demonstrations of select-examples of beamforming using the proposed unit cell to illustrate its reflection engineering capabilities in spite of limited magnitude-phase coverage. Sec. V presents practical implementation considerations and experimental demonstration of a PIN-based reflector for magnitude-only beamforming, a varactor-based reflector for phase-only beamforming, and finally a combined varactor/PIN-based reflector for simultaneous magnitude and phase beamforming. Conclusions are provided in Sec. VI.

II. PROPOSED COUPLED RESONATOR UNIT CELL

The proposed unit cell along with an illustration of a beamforming example are shown in Fig. 1. The proposed unit cell is sub-wavelength (i.e., $\Lambda < \lambda_0$ at the design frequency) with two strongly coupled resonators for complex reflectance control. The unit cell is composed of an SRR with a capacitive element, C, and a DRR with a resistive element, R. The unit cell was developed from an evolution starting from a single resonator that is adapted for practical implementation using active components with DC isolation between the components' bias points as shown in Fig. 2. The following investigations are based on Ansys FEM-HFSS periodic Floquet simulations with ideal R and C boundaries.

A single resonator provides excellent control of magnitude and phase by tuning the resistance, R, and capacitance, C, respectively, as shown in Fig. 2(a). However this unit cell is sensitive to variations in the resistance and more importantly it is not suitable for implementation with active elements that require DC biasing since the two lines are not DC-isolated. This issue can be resolved by introducing gaps in the resonator to isolate the lines for each component as shown in Fig. 2(b). The addition of these gaps introduces a physical separation of the two halves of the SRR, and one may view them as two dipoles placed in close proximity to each other, i.e., an early sign of a coupled resonator configuration. This now adds a new dimension of coupling which must now be properly engineered. The response in Fig. 2(b) shows poor coupling as evident by the limited magnitude control range. As an attempt to improve coupling, cuts were extended to increase the area over which the two resonators are coupled as shown in Fig. 2(c). This results in improved coupling as the magnitude range is significantly enhanced, however the phase response becomes very sensitive to small variations in capacitance, which is not ideal for practical implementation. An alternative configuration, but with the same aim of achieving an optimized coupling, is to use two coupled SRRs, one inside the other as shown in Fig. 2(d). While the phase response stabilized with changes in capacitance, the magnitude variation remains limited.

These examples have demonstrated that to achieve magnitude and phase coverage from two DC-isolated tunable elements, each element must control a physically separate resonator and the coupling between them must be properly engineered to achieve enhanced control over the magnitude and phase. With this in mind, a unit cell based two physically separate resonators is proposed here. The proposed unit cell is based on an outer SRR with a capacitive element and an inner DRR with a resistive element as shown in Fig. 3. As will be shown, this unit cell provides the best trade-off between sensitivity to capacitance/resistance values and enhanced complex reflectance coverage.

First, a unit cell without DC-isolation consideration at each resonator level is investigated as shown in Fig. 3(a), as the ideal case. This unit cell shows control over magnitude and phase by controlling the values of C and R as shown in Fig. 3(b). Fig. 3(c) & (d) further show excellent control over the complex reflectance, in rectangular and Smith Chart plots respectively, at the design frequency chosen to be $f = 8.8$ GHz in this example. Next, a practical unit cell with DC-isolation at each resonator level, achieved through adding gaps in the resonators, is investigated as shown in Fig. 3(e). Fig. 3(f) shows magnitude and phase control similar to before with controlled sensitivity to variations in the resistance and capacitance values. This however comes with a reduced complex reflectance coverage at the design frequency ($f = 10$ GHz, in this example) as shown in Fig. 3(g) & (h). Despite the reduced complex reflectance control, this unit cell exhibits practically acceptable beamforming capabilities, achievable through both magnitude and phase control, such as asymmetrical multi-beam patterns, as will be demonstrated with full-wave and experimental results in the next sections.

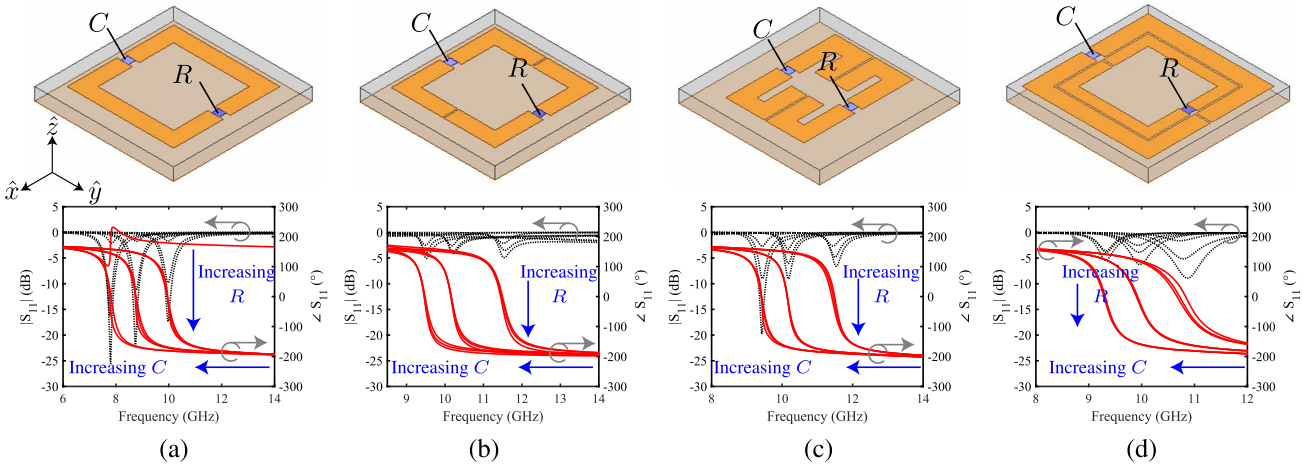

FIGURE 2. Ansys FEM-HFSS full-wave Floquet (complex reflectance) results of single and coupled resonators for magnitude and phase control. (a) Single resonator ($C = 0.1$ to 2.2 pF, $R = 0$ to 10 Ω), (b) single resonator with cuts for DC isolation ($C = 0.1$ to 0.3 pF, $R = 0$ to 200 Ω), (c) single resonator with cuts for DC isolation with extended coupling area ($C = 0.1$ to 0.3 pF, $R = 0$ to 20 Ω), and (d) coupled SRRs ($C = 0.1$ to 2.2 pF, $R = 0$ to 200 Ω).

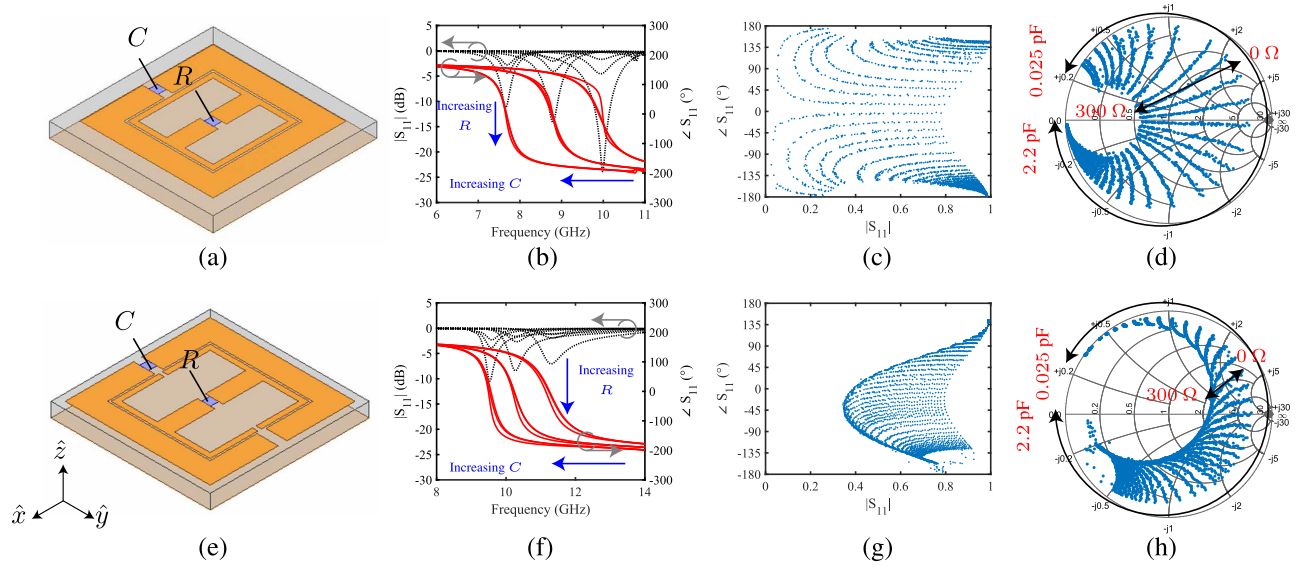

FIGURE 3. Ansys FEM-HFSS full-wave Floquet (complex reflectance) results of the proposed coupled resonator unit cell based on an SRR and a DRR. (a) Coupled resonator without DC isolation, (b) complex reflectance as a function of frequency for three values of $C = 0.1$ to 2.2 pF and three values of $R = 0$ to 100 Ω, (c) & (d) complex reflectance at $f = 8.8$ GHz for various values of C and R. (e) Coupled resonator with DC isolation, (f) complex reflectance as a function of frequency for three values of $C = 0.1$ to 2.2 pF and three values of $R = 0$ to 200 Ω, (g) & (h) complex reflectance at $f = 10$ GHz for various values of C and R.

Note that, in principle, an attempt can be made to regain the enhanced complex reflectance coverage using three high-value capacitors at the locations of the physical gaps while maintaining the DC isolation. However losses and other parasitic effects may adversely impact the RF performance, in addition to the added cost of the extra components which is an issue we are trying to minimize in our proposed design for simplicity and practicality.

III. THEORETICAL ANALYSIS

To gain better insight into this coupling phenomenon, the unit cell is next investigated using the Lorentz oscillator model to reproduce the frequency-dependent response of the unit cell. In this model, a generic metasurface unit cell with coupled resonances can be described using its frequency-dependent constitutive parameters. A very convenient way to describe them is to use the effective surface susceptibility model in conjunction with zero thickness generalized sheet transition conditions (GSTCs) [34]. The frequency dependence can be assigned using a Lorentz oscillator model, so that the complex electric susceptibility of the unit cell can be written as a sum of n resonances given by [35]

$$\chi_{ee}(\omega) = a_0 + \sum_{i=1}^{n} \frac{\omega_{p,i}}{\omega_{0,i}^2 - \omega^2 + j\gamma_i\omega}, \tag{1}$$

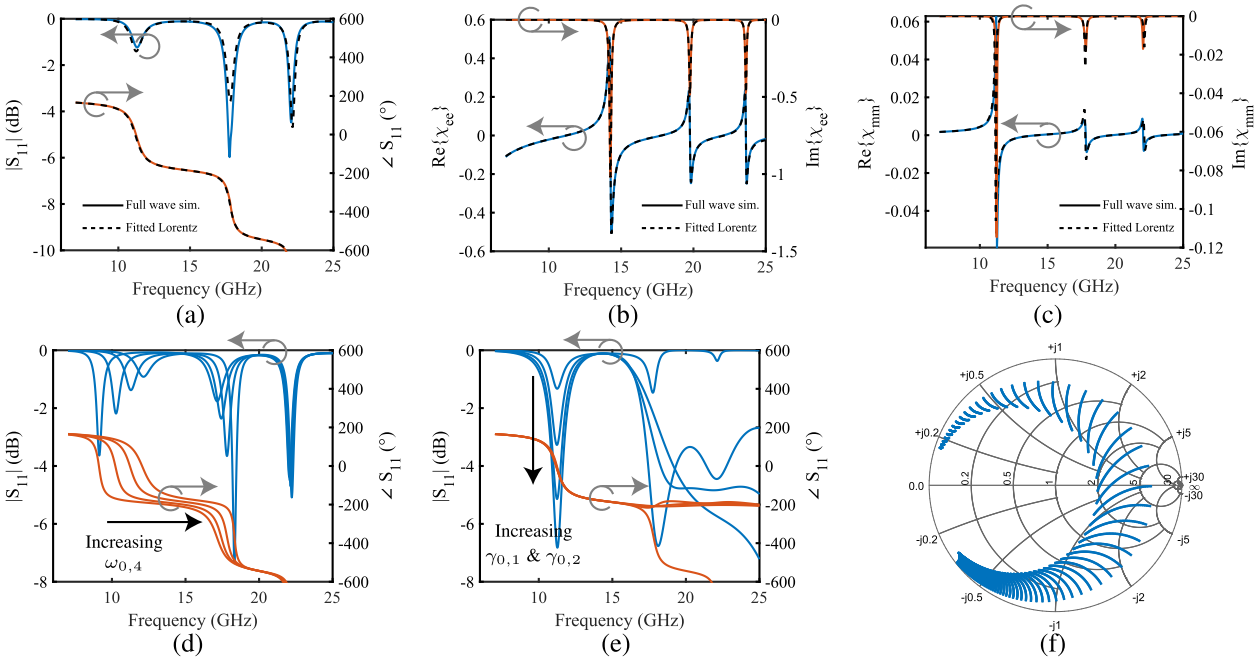

FIGURE 4. Results of the theoretical analysis of the proposed coupled resonator unit cell using a Lorentz oscillator model. Full-wave and Lorentz-fitted results are shown for the (a) reflection coefficient, (b) electric susceptibility, and (c) magnetic susceptibility. The full-wave results are those of the coupled resonator in Fig. 3(c) with $C = 0.1$ pF and $R = 0\ \Omega$. The fitted Lorentz parameters are $a_0 = 0.015$, plasma frequencies $\omega_{p,i} = \{4.89, 5.23, 22.7, 8.39\} \times 10^{19}$ rad/s, resonance frequencies $\omega_{0,i} = 2\pi\{23.6, 19.8, 2.97, 14.3\}$ Grad/s, damping coefficients $\gamma_{0,i} = \{0.69, 0.88, 0.1, 0.94\} \times 10^9$. (d) Effect of varying the resonance frequency, $\omega_{0,4}$, between $2\pi(11)$ Grad/s and $2\pi(16)$ Grad/s, (e) effect of varying the damping coefficients, $\gamma_{0,1}$ and $\gamma_{0,2}$, between 0 and 157×10^9 (both with the same values), and (f) effect of varying $\omega_{0,4}$, $\gamma_{0,1}$, and $\gamma_{0,2}$ at $f = 10$ GHz.

where a_0 is a constant, $\omega_{p,i}$ are the plasma frequencies, $\omega_{0,i}$ are the resonance frequencies, and γ_i are the damping coefficients. For the case under investigation with normal incidence excitation, the transmission coefficient, $S_{21} = 0$. This leads to inter-dependent electric and magnetic surface susceptibilities which have the following relationship at each frequency:

$$\chi_{\text{mm}}(\omega) = -\frac{4}{k_0^2}\chi_{\text{ee}}(\omega). \tag{2}$$

The electric and magnitude surface susceptibilities, χ_{ee} and χ_{mm} respectively, can be calculated from the S-parameters under normal incidence as follows [36]

$$\chi_{\text{ee}}(\omega) = \frac{2j}{k_0}\left[\frac{S_{21}(\omega) + S_{11}(\omega) - 1}{S_{21}(\omega) + S_{11}(\omega) + 1}\right], \tag{3a}$$

$$\chi_{\text{mm}}(\omega) = \frac{2j}{k_0}\left[\frac{S_{21}(\omega) - S_{11}(\omega) - 1}{S_{21}(\omega) - S_{11}(\omega) + 1}\right], \tag{3b}$$

where $k_0 = \omega/c$ is the free-space wavenumber, and $S_{21} = 0$ at all frequencies, as mentioned earlier.

The results of the investigation are shown in Fig. 4. First the S-parameters are simulated in a wide bandwidth for one variation of the coupled resonator unit cell, and the electric and magnetic susceptibilities are extracted using Eq. (3). The susceptibilities calculated using the Lorentz oscillator model from Eq. (1) are then curve fitted to determine the plasma frequencies, resonance frequencies, and damping coefficients. Full-wave and Lorentz-fitted results are shown in Fig. 4(a)-(c). It was found that the response can be modeled with four resonances, three of which are of interest to the model. One resonance around 10 GHz is considered to be produced by the SRR and the other two resonances between 15 and 25 GHz are considered to be produced by the DRR. Varying the SRR's resonance frequency (e.g., using a varactor control) controls the phase near the SRR resonance around 10 GHz, as shown in Fig. 4(d), while varying the damping coefficient of the two DRR's resonances (e.g., using a PIN diode) controls the magnitude at the design frequency, as shown in Fig. 4(e). The effect of varying all three parameters (one resonance frequency and two damping coefficients) at the design frequency, $f = 10$ GHz, is shown in Fig. 4(f), a response that is qualitatively similar to the one obtained from full-wave simulations in Fig. 3(h). This indicates that the Lorentz oscillator model provides an appropriate physical description of the underlying operation of the proposed coupled resonator unit cell.

IV. FULL-WAVE DEMONSTRATION

Next, we will demonstrate complex beamforming in full-wave simulations utilizing the simultaneous magnitude-phase control characteristics of the proposed unit cell. A 1-D array of the unit cell was used for this demonstration as shown in Fig. 5. It consists of N number of unit cells with varying ideal R and C element values across the array.

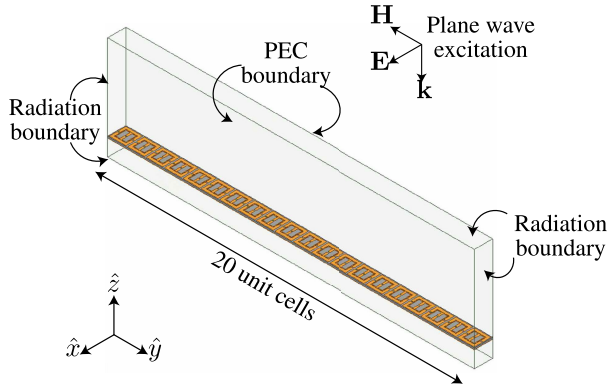

FIGURE 5. Illustration of a full-wave setup on Ansys FEM-HFSS for 1-D beamforming from a 20 × 1–unit cell array of the proposed unit cell with an *x*–polarized normally-incident plane wave.

A linearly-polarized uniform plane wave is used to excite the structure, with perfect electric conductor (PEC) boundary conditions on the two broad walls. Radiation boundaries are used to capture the finite extent of the array on both sides.

To achieve a variety of beamforming operations, simple array factor calculations were used to determine the complex reflectance of the aperture fields under normal plane wave excitation. Several examples are considered: a single beam-steering, side-lobe level control, single beam-steering with gain control, and finally dual-beam generation with asymmetric placements. Note that the last two beamforming examples cannot be generated using phase-only or magnitude-only control metasurfaces, i.e., a complex reflectance control is required. These several beamforming examples are shown in Fig. 6. An acceptable match is found between the ideal array factor patterns (labeled "Ideal AF"), the patterns obtained using the array factor and the achievable complex reflectance from the coupled resonator (labeled "CR - AF"), and the full-wave simulation patterns (labeled "CR - HFSS") obtained using the setup in Fig. 5, in all cases. We remark here that very effective beamforming is achievable even when the overall complex reflectance coverage was compromised based on practical considerations as mentioned earlier and demonstrated in Fig. 3. The various differences observed in Fig. 6 may be attributed to mutual coupling, edge diffraction, and element pattern effects, all of which are not taken into account by the array factor.

An important characteristic of any device is its operation bandwidth, which is next investigated. The directivity versus angle and frequency is plotted for three beamforming cases as shown in Fig. 7, where, at each frequency, the directivity is normalized with respect to the peak directivity of a PEC reflector of the same size as the metasurface reflector, illuminated by a normally-incident plane wave. For the beam-steering case of Fig. 7(a), the bandwidth is defined as the frequency range where the steered beam is within 3 dB of its peak value of −3 dB (i.e., −6 dB with respect to the PEC reflector) and no other beam has more power than the desired steered beam. For the SLL reduction case of Fig. 7(b), the beamwidth is defined as the frequency range were the SLLs are below −20 dB with respect to the PEC reflector. Finally, for the dual-beam case of Fig. 7(c), the bandwidth is defined as the frequency range where both beams are within 3 dB of their peak values of −7 and −13 dB (overall −10 and −16 dB), for the beams at $\theta = 0°$ and $\theta = 30°$, respectively. The typical operation bandwidths under ideal conditions range from 300 MHz to 700 MHz (about 3% to 7% fractional bandwidths) as indicated in Fig. 7.

V. EXPERIMENTAL DEMONSTRATION

A. PRACTICAL DESIGN CONSIDERATIONS

To demonstrate the proposed metasurface reflectors, a systematic approach is adopted starting from PIN-only and varactor-only designs for magnitude-only or phase-only control, respectively. For the sake of reducing biasing complexity and to limit the number of required DC channels (limited by the available hardware in our experimental facility), reflectors were designed for single-plane beamforming with biasing on a column-by-column basis. However the same unit cell can simply be used in a configuration where each unit cell is individually biased to achieve beamforming in two orthogonal planes. This is considered a tedious implementation, but conceptually straightforward extension of this structure. The end-surface is a combined coupled resonator configuration for simultaneous magnitude and phase control.

A practical implementation must include DC bias lines and RF-DC isolation at each unit cell to avoid loading the resonator with the DC lines. High impedance points can be created at the points of contact between the DC lines and active components using RF choke (RFC) inductors or radial stubs. While using RFCs is a simple technique to achieve RF-DC isolation, it is not easily scalable to higher frequencies, is limited to component availability, and adds parasitics and cost. On the other hand, stubs are cheaper and less susceptible to tolerance beyond that of PCB fabrication, so they were chosen for this implementation. However, as will be seen later, it is challenging to include multiple radial stubs inside the small sub-wavelength region of the unit cell to bias each of the active components used. Thus a reduction in number of active elements is needed for greater simplicity and feasibility unless RFCs are used.

Keeping in mind future extension to full 3D beamforming requiring cell-by-cell biasing and to minimize any interaction between the DC biasing network and the incoming wave excitation of the surface, the biasing network was placed on a separate layer behind the ground plane of the metasurface reflector. This also ensures that the metasurface functionality (e.g., polarization handling) and the biasing network functionally are electromagnetically isolated and thus can be designed completely independently. As a result, the reconfigurable reflectors presented here are fabricated with a multi-layer PCB as shown in Fig. 8 for the PIN-based [Fig. 8(a)], varactor-based [Fig. 8(b)], and

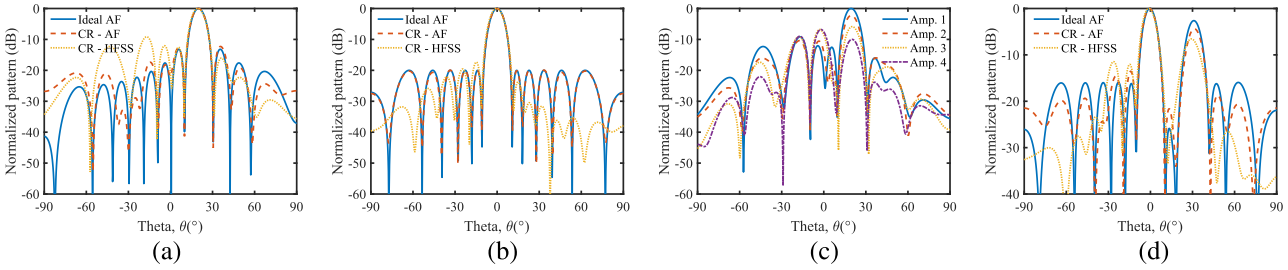

FIGURE 6. Ansys-FEM full-wave demonstration of beamforming using the proposed coupled resonator (CR) unit cell. Beamforming examples shown are (a) beam-steering, (b) SLL reduction, (c) beam-steering with amplitude control, and (d) asymmetrical dual-beam pattern. The legends denote radiation patterns determined using ideal array factor (AF) calculations, "Ideal AF", array factor calculations using the proposed coupled resonator values of complex reflectance, "CR - AF", and full-wave simulations with ideal *R* and *C* values corresponding to the required complex reflectance, "CR - HFSS".

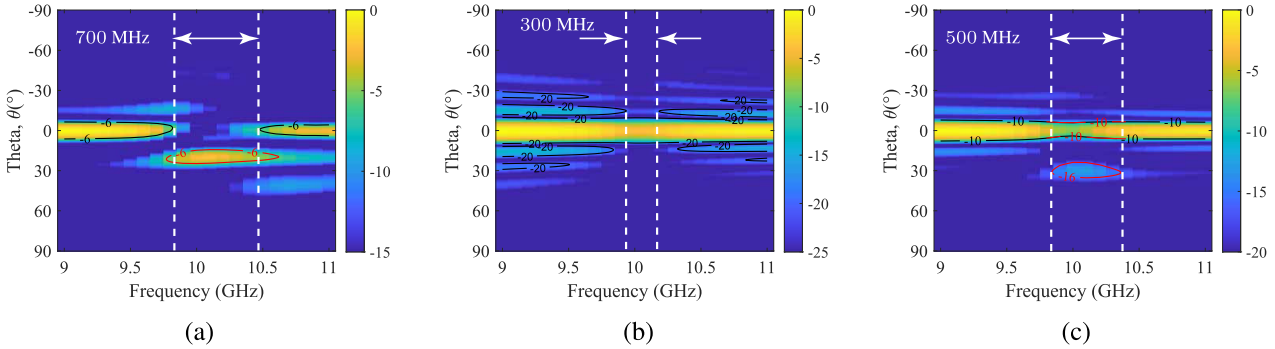

FIGURE 7. Bandwidth investigation using 2-D plots of normalized directivity as a function of angle and frequency for three cases from the beamforming demonstration in Fig. 6. (a) beam-steering, (d) SLL reduction, and (c) asymmetrical dual-beam pattern.

varactor/PIN-based unit cells [Fig. 8(c)]. Metallized vias were used to route the DC signals from the bottom biasing layer through the ground plane to the two terminals of the active circuit elements to provide appropriate biasing conditions corresponding to the specific component used.

For the unit cells, their designs were based on practical varactor and PIN diode elements. Thus the unit cells were redesigned with the thru-reflect-line (TRL)-characterized touchstone s2p files of off-the-shelf SMV2019-040LF varactor diodes [37] and the SMP1302-040LF PIN diodes [38]. It should be noted that this is in contrast to equivalent circuit models typically being used to design these structures in the literature [39], [40], [41], which are only approximate. A co-designed unit cell with experimentally-characterized touchstone files represent the most favorable approach to design these structures, which is thus followed in this work.

B. PIN-BASED METASURFACE REFLECTOR

The first surface to be demonstrated is a metasurface reflector with magnitude-only control. It is a 15 × 10–unit cell array, configured for biasing on a column-by-column basis, along 15 columns each with 10 unit cells, as shown in Fig. 9(a) & (b). The unit cell consists of DRR loaded with a PIN diode. The array of DRRs in a single column are biased identically, so that each PIN diode is driven with the same current (i.e., a series configuration), thus offering a tunable resistance. This allows for magnitude variation along the $y-$direction while being constant along the $x-$direction, i.e., beamforming in the $yz-$plane. Furthermore, two radial stubs are used in each cell in the bottom biasing layer, providing RF-DC isolation directly at the unit cell level as illustrated in Fig. 8(a).

The radiation patterns were measured in a bi-static measurement setup as shown in Fig. 9(c). The measurement setup consists of two antennas (a parabolic dish and a horn), the metasurface reflector under test, and a VNA. The parabolic dish and the horn are connected to Ports 1 and 2 of the VNA. The parabolic dish is fixed at normal incidence, and the horn rotates on a circular path centered on the position of the reflector located a distance of $r_0 = 1.2$ m away from the horn and the dish. It should be noted that this puts constraints on the size of the reflector and does not strictly satisfy the far-field conditions required for ideal operation. To measure the reflection radiation pattern of the reflector, the equivalent transmission coefficient, S_{21}, is monitored as a function of angle, i.e., $S_{21}(\theta, \phi = 90°, \omega)$.

The first step in the reflector measurement is the generation of the look-up table. A look-up table for bias currents versus complex reflectance is first generated by measuring the transmission coefficient of a uniformly-biased surface at different bias points and at normal incidence (i.e., the horn and the dish are pointing directly at the surface, with the horn at $\theta = 0°$). Fig. 9(d) & (e) show the measured transmission magnitude and phase respectively, for

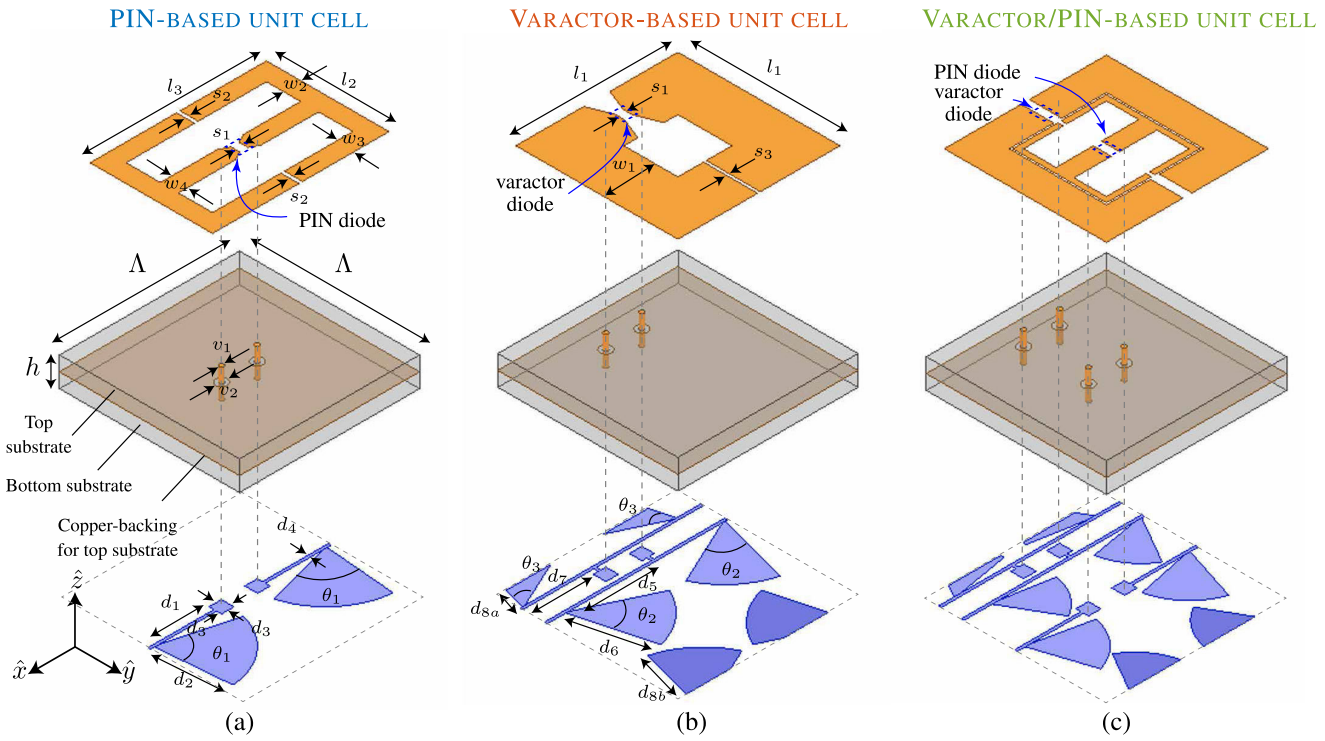

FIGURE 8. Practical multi-layer implementation of metasurface reflectors based on active components with RF-DC isolation using radial stubs. In all cases, the unit cell period is $\Lambda = 10$ mm. (a) PIN-based unit cell (dimensions in mm: $l_2 = 6.8$, $l_3 = 9.8$, $s_1 = 0.4572$, $s_2 = 0.2$, $w_2 = 1$, $w_3 = 1$, $w_4 = 1$, $v_1 = 0.254$, $v_2 = 0.635$, $d_1 = 3.3$, $d_2 = 4.1$, $d_3 = 0.7$, and $d_4 = 0.1542$, and stub angle $\theta_1 = 70°$), (b) varactor-based unit cell (dimensions in mm: $l_1 = 9$, $s_1 = 0.4572$, $s_3 = 0.1542$, $d_5 = 4.8$, $d_6 = 4.4$, $d_7 = 3.7$ and $d_8 = d_{8a} + d_{8b} = 1.3 + 3.1 = 4.4$, and stub angles $\theta_2 = \theta_3 = 50°$), and (c) varactor/PIN-based unit cell (dimensions in mm, see Fig. 1: $l_1 = 9$, $l_2 = l_3 = 5.2$, $s_1 = 0.4572$, $s_2 = 0.2$, $s_3 = 0.5$, $w_1 = 1.8$, $w_2 = w_3 = 0.3$, $w_4 = 1$) using the same stubs from (a) & (b). The unit cell is implemented on a multi-layer PCB with a total height of $h = 1.83$ mm, comprising of a top copper-backed Rogers RO4003C substrate ($\epsilon_r = 3.55$, $\tan\delta = 0.0027$, and height, $h_1 = 32$ mil), a bottom Rogers RO4003C substrate with height, $h_2 = 32$ mil, and a prepreg FR4 layer with height, $h_3 = 0.2$ mm sandwiched between the two Rogers' substrates.

varying uniform currents through PIN diodes in all columns. Fig. 9(f) & (g) show the complex transmittance at the chosen design frequency of $f = 11$ GHz, where magnitude control is evident with small phase variation. This data can now be used to determine the bias current required for each column to achieve any beamforming based on magnitude variation.

Next, the radiation patterns are measured. A copper sheet of the same size as the reflector was first measured to serve as a reference to quantify the loss in the metasurface. The measured radiation pattern of the copper sheet and the PIN-based reflector with uniform current bias to all columns are shown in Fig. 9(h). It is evident that the PIN-based reflector suffers $\approx$ 3 dB reduction in peak reflected power when compared to the copper sheet, without any beamforming.

Beamforming examples are next demonstrated. Control over the beam amplitude is shown in Fig. 9(i) by uniformly biasing the surface with different currents that correspond to varying reflection magnitudes determined by the look-up table. Next, SLL reduction is demonstrated in Fig. 9(j), where the weights were determined by applying a Dolph-Chebyshev amplitude tapering [42]. Compared to the same surface with uniform currents (i.e., no beamforming), the SLL reduction suffers from $\approx$ 2 dB drop in peak amplitude. This is expected since reducing the SLL results in less directive radiation. Another beamforming demonstration is shown in Fig. 9(k) by applying binary amplitude grating (highest reflection, 1, and lowest reflection, 0, points) on the surface. Binary amplitude grating generates three symmetrical beams, whose angles depend on the periodicities of the amplitude grating applied. These results thus show the capability of the PIN-based metasurface reflector for controlling the reflection magnitude over the aperture, as demonstrated through various beamforming examples.

C. VARACTOR-BASED METASURFACE REFLECTOR

Next, a varactor-based metasurface reflector will be demonstrated for controlling the reflection phase over the aperture. The fabricated varactor-based metasurface reflector and its measured results are shown in Fig. 10. It is a 15 $\times$ 10–unit cell array, configured for biasing on a column-by-column basis, along 15 columns each with 10 unit cells, as shown in Fig. 10(a) & (b). The unit cell consists of an SRR loaded with a single varactor diode. The varactor diodes are biased through two vias connecting them to the DC lines on the bottom biasing layer. Since varactor are voltage-controlled devices, and are used in a column-by-column configuration, they are biased in the parallel configuration. This requires

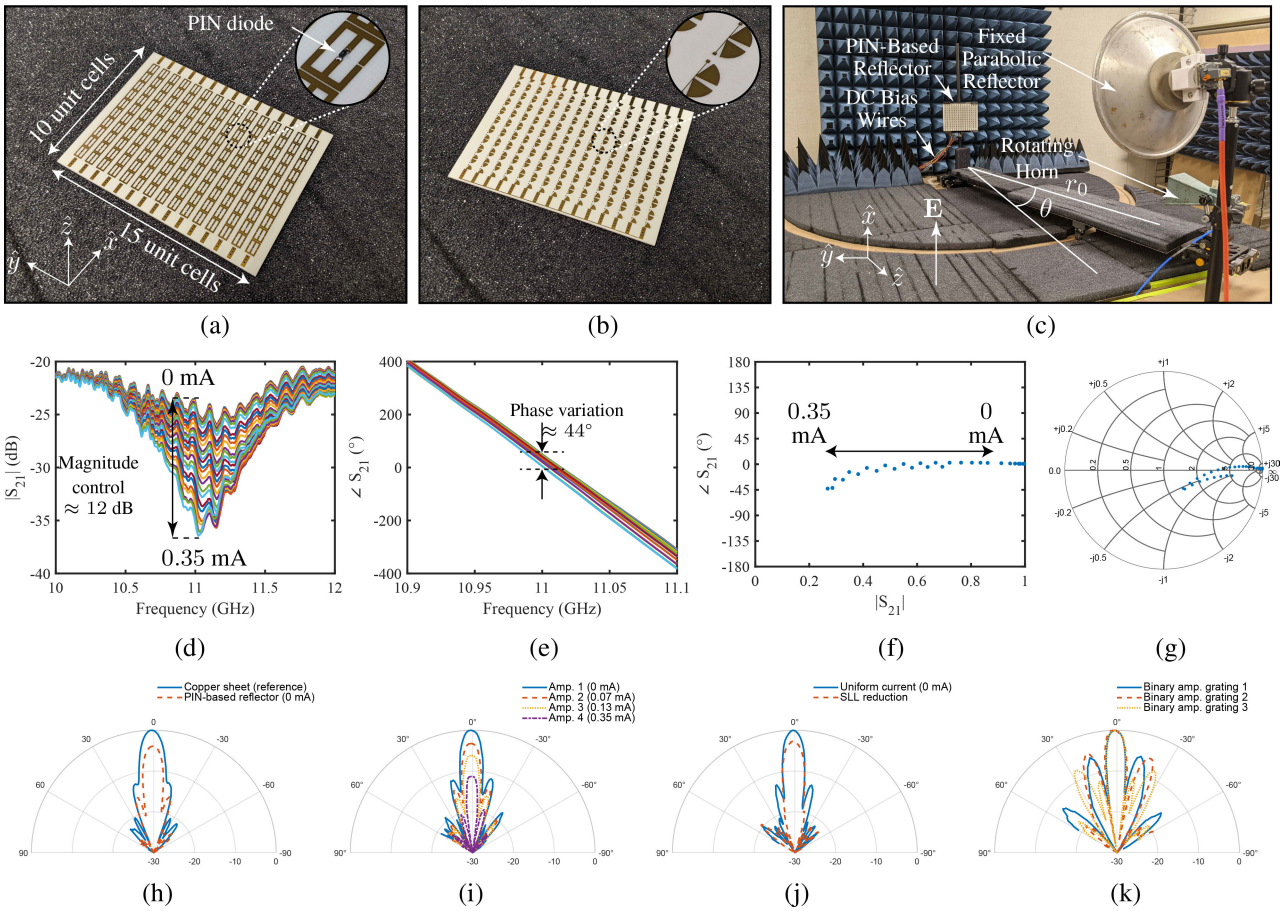

FIGURE 9. Experimental demonstration of the PIN-based metasurface reflector. (a) Top and (b) bottom views of the metasurface reflector. (c) Experimental setup. (d) Measured transmission coefficient magnitude and (e) phase with normal incidence. (f) & (g) Complex transmittance at $f = 11$ GHz. (h) Measured radiation pattern at $f = 10$ GHz of a copper sheet and the metasurface reflector with uniform maximum magnitude using 0 mA for all columns. (i) Measured radiations patterns at $f = 11$ GHz demonstrating amplitude control using different uniform current levels. (j) Measured radiation pattern at $f = 11.2$ GHz demonstrating SLL reduction by varying current levels in each column, compared to the radiation pattern with 0 mA for all columns. (k) Measured radiation patterns at $f = 11.3$ GHz demonstrating three cases of binary amplitude grating.

two DC lines, one for a common DC ground and another for the voltage bias, as shown in the inset of Fig. 10(b). Moreover, two radial stubs are used per DC lines for RF-DC isolation, i.e., four stubs per unit cell area as illustrated in Fig. 8(b).

The radiation patterns were next measured as shown in Fig. 10(c), with the same measurement setup as previously discussed. The first step was to generate the look-up table. A look-up table for bias voltage versus complex transmittance is generated by measuring the transmission coefficient at different bias points and at normal incidence (i.e., the horn and the dish are pointing directly at the surface, with the horn at $\theta = 0°$). Fig. 10(d) & (e) show the measured transmission magnitude and phase respectively, for varying uniform voltages through all varactor diode columns. Fig. 10(f) & (g) show the complex transmittance at the chosen design frequency of $f = 10.3$ GHz, where phase control is evident with noticeable magnitude variation, which is to be expected due to the resonance nature of the design. This data can now be used to determine the bias voltage required for each column to achieve any beamforming based on phase variation.

Next, the radiation patterns are measured. As previously done, a copper sheet of the same size as the reflector was measured to serve as a reference to quantify the loss in the metasurface. The measured radiation patterns of the copper sheet and the varactor-based reflector with uniform voltage bias to all columns are shown in Fig. 10(h). It is evident that the varactor-based reflector suffers ≈ 2 dB reduction in peak reflected power when compared to the copper sheet, without any beamforming.

Beamforming examples are next demonstrated. One beam-steering demonstration is shown in Fig. 10(i). This was achieved through selecting specific voltage bias points for each column to achieve the required phase variation for tilting the normally-incident beam. Compared to the surface with uniform voltage, the tilted beam suffers from ≈ 4 dB reduction in peak power, which is partially attributed to component loss and partially due to scan loss from the element pattern. Two additional beam-steering cases are

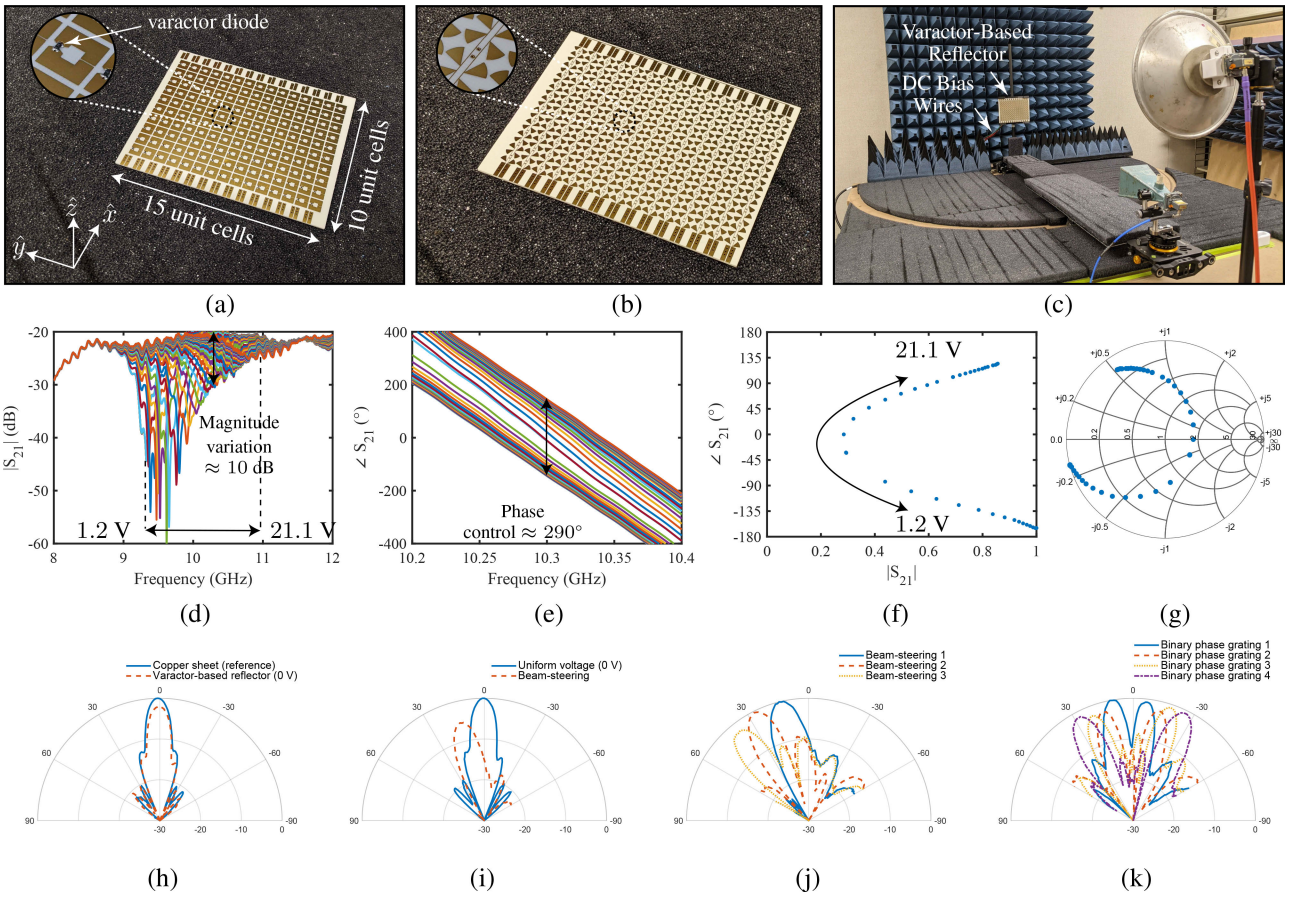

FIGURE 10. Experimental demonstration of the varactor-based metasurface reflector. (a) Top and (b) bottom views of the metasurface reflector. (c) Experimental setup. (d) Measured transmission coefficient magnitude and (e) phase with normal incidence. (f) & (g) Complex transmittance at $f = 10.3$ GHz. (h) Measured radiation pattern at $f = 10$ GHz of a copper sheet and the metasurface reflector with uniform voltage level of 0 V for all columns. (i) Measured radiations patterns at $f = 10.3$ GHz demonstrating beam-steering, compared to the radiation pattern with 0 V for all columns. (j) Measured radiation pattern at $f = 10.3$ GHz demonstrating three different beam-steering cases. (k) Measured radiation patterns at $f = 10.3$ GHz demonstrating four cases of binary phase grating.

shown in Fig. 10(j) demonstrating versatile control over the beam angle. A final beamforming demonstration is shown in Fig. 10(k) by applying binary phase grating (0° and 180° points) on the surface. Binary phase gratings generate two symmetrical beams, whose angles depend on the periodicities of the phase grating applied. This is analogous to the 1-bit metasurface where the same effect is achieved using two discrete operation states of a PIN diode [43].

These results have shown the capability of the varactor-based metasurface reflector for controlling the reflection phase over the aperture, as demonstrated through various beamforming examples, and have verified the basic operation of two individual resonators with either varactor or PIN diode loading. Next, the combined varactor/PIN-based metasurface reflector, based on the proposed unit cell, will be demonstrated for simultaneously controlling the reflection magnitude and phase over the aperture. The varactor/PIN-based metasurface reflector will also be used to achieve rich transformations such as beam-steering with amplitude control and asymmetrical multi-beam patterns.

D. VARACTOR/PIN-BASED COUPLED RESONATOR METASURFACE REFLECTOR

The final demonstration is a combined varactor/PIN diode design for complex reflectance control. The fabricated varactor/PIN-based metasurface reflector and its measured results are shown in Fig. 11. It is a 15 × 10–unit cell array, configured for biasing on a column-by-column basis along 15 columns each with 10 unit cells as shown in Fig. 11(a) & (b). Similar to the previous two prototypes, the column-by-column controls include series-connected PIN diodes and parallel-connected varactor diodes. This necessitates one DC bias line for PIN diodes with two radial stubs per unit cell, and two DC bias lines for varactor diodes with four radial stubs per unit cell. That is a total of six radial stubs per unit cell area, as illustrated in Fig. 8 and shown in the inset of Fig. 11(b).

The radiation patterns were measured as shown in Fig. 11(c), with the same measurement setup as the two previous demonstrations with the PIN-based and varactor-based reflectors. As usual, a look-up table for bias voltage

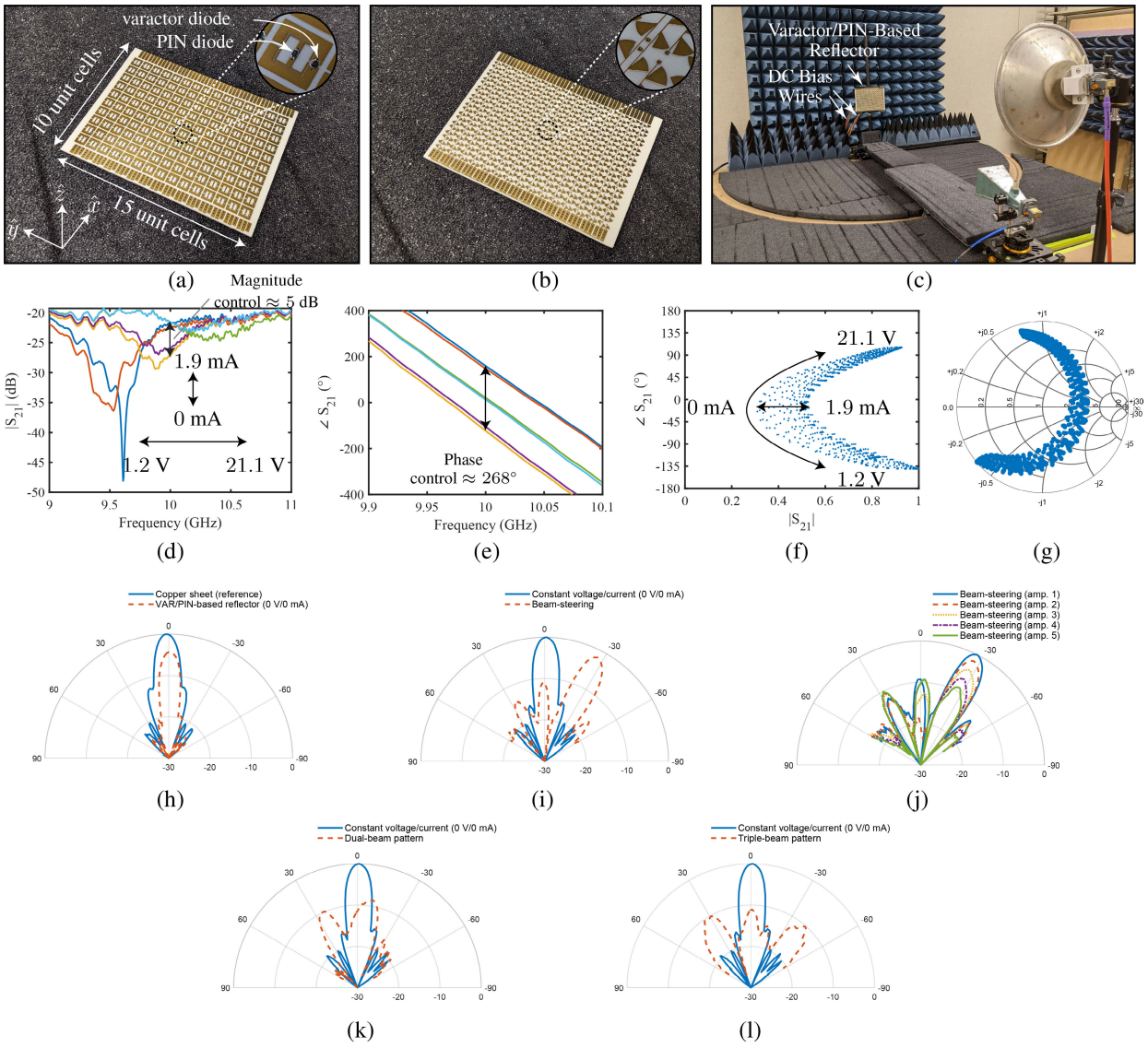

FIGURE 11. Experimental demonstration of the varactor/PIN-based metasurface reflector. (a) Top and (b) bottom views of the metasurface reflector. (c) Experimental setup. (d) Measured transmission coefficient magnitude and (e) phase with normal incidence. (f) & (g) Complex transmittance at $f = 10$ GHz. (h) Measured radiation pattern at $f = 10$ GHz of a copper sheet and the metasurface reflector with uniform voltage level of 0 V for all varactor diodes and a uniform current level of 0 mA for all PIN diodes. (i) Measured radiations patterns at $f = 10$ GHz demonstrating beam-steering, compared to the radiation pattern with 0 V and 0 mA for all columns. (j) Measured radiation patterns at $f = 10$ GHz demonstrating beam-steering with five amplitude cases. (l) Measured radiation pattern at $f = 10$ GHz demonstrating a dual-beam pattern. (l) Measured radiation pattern at $f = 10$ GHz demonstrating a triple-beam pattern.

and current versus complex transmittance is first generated by measuring the transmission coefficient at different bias points and at normal incidence (i.e., the horn and the dish are pointing directly at the surface, with the horn at $\theta = 0°$). Fig. 11(d) & (e) show the measured transmission magnitude and phase respectively, for three uniform voltages across all varactor diodes, and two uniform currents through all PIN diodes. Fig. 11(f) & (g) show the complex transmittance at the chosen design frequency of $f = 10$ GHz, where phase control is achieved with varying voltage (due to varactor diode tuning), and magnitude control is achieved with varying current (due to PIN diode tuning). This data can be used to determine bias voltages and currents required for each column to achieve any beamforming based on both magnitude and phase variation.

Next, the radiation patterns are measured. As previously done, a copper sheet of the same size as the reflector was measured to serve as a reference to quantify the loss in the metasurface. The measured radiation patterns of the copper sheet and the varactor/PIN-based reflector with uniform voltage and current bias, 0 V and 0 mA respectively, to all columns are shown in Fig. 11(h). It is evident that the reflector suffers $\approx$ 4 dB reduction in peak reflected power when compared to the copper sheet, without any beamforming.

Beamforming examples are next demonstrated. One beam-steering demonstration is shown in Fig. 11(i). This was achieved through selecting specific voltage bias points for each column to achieve the required phase variation for tilting the normally-incident beam. Compared to the surface with uniform voltage, the tilted beam suffers from $\approx$ 2 dB

reduction in peak power. This is partially due to component loss and partially due to scan loss due to the element pattern. The same beam-steering case is now used to demonstrate magnitude control as shown in Fig. 11(j), which illustrates fine control over the beam amplitude by varying the bias current while maintaining the bias voltage for beam-steering. Two additional beamforming cases are demonstrated; an asymmetrical and unbalanced dual-beam pattern as shown in Fig. 11(k), and a symmetrical triple-beam pattern as shown in Fig. 11(l). Both patterns exhibit $\approx$ 10 dB drop in peak power compared to the uniform surface, which is mainly due to the power sharing between the multiple beams, in addition to component loss and element pattern scan loss, as previously discussed.

We should recall that the last three beamforming cases cannot be achieved using either phase-only or magnitude-only reflectors, and a complex reflectance control is a necessary requirement. Furthermore, the reflector is capable of generating reflection patterns of multi-beams to near-arbitrary profiles subject to achievable magnitude-phase characteristics. These results have demonstrated the capability of the proposed coupled resonator unit cell in a varactor/PIN-based metasurface reflector for controlling the complex reflectance over the aperture, as demonstrated through various beamforming examples.

VI. CONCLUSION

A novel metasurface reflector unit cell based on coupled resonators with two dynamic controls; an SRR with a varactor diode and a DRR with a PIN diode, was proposed and demonstrated for beamforming applications. The unit cell was developed from an evolution of a single resonator adapted for practical implementation with active components by physically isolating the lines to allow for isolated DC bias points. Beamforming capabilities of the unit cell were demonstrated in full-wave simulations. Three metasurface reflector prototypes were fabricated and measured. A varactor-based metasurface reflector was used to demonstrate beamforming through phase control. A PIN-based metasurface reflector was used to demonstrate beamforming through magnitude control. A varactor/PIN-based metasurface reflector was used to demonstrate beamforming through both magnitude and phase control.

While single-plane beamforming was demonstrated here for experimental simplicity by biasing on a column-by-column basis, the proposed reflector architecture is easily extendable to two-plane beamforming by individual biasing of each unit cell. This is considered a straightforward extension of this reflector as the biasing network is isolated from the illumination side of the reflector. The gain in beamforming capabilities of this approach is clear, however it comes at the expense of harsh requirements on digital-to-analog converters (DACs) due to the need for a large number of bias lines when a practical metasurface is eventually implemented with a microcontroller for programmable reconfigurability. This however can be considered as a common challenge in general dynamic metasurface reflector designs that must be handled with special care where multiple active components are introduced in the unit cell.

Another practical extension of this work is to include polarization control, following the supercell concept as proposed in [44] and [45]. Future work will also focus on retrieving some of the lost magnitude-phase coverage when DC isolation gaps are introduced into the unit cell. This may involve either using static lumped capacitors (not preferred, if possible, due to increased number of circuit components with undesired parasitic effects and increased cost), or printed high frequency DC block capacitors compatible with the printed circuit board fabrication process. The proposed metasurfaces thus represent an important step in achieving a fully reconfigurable reflector system that can be scaled to larger surface areas and frequencies providing a near complete control over their reflected fields. This will benefit several application areas where the proposed unit cell represents a versatile and a practical building block for designing reconfigurable reflectors to engineer EM waves in wireless environments, especially in the context of 5G and near-line-of-sight communication. In addition, they may find potential applications in satellite communications in the form of reconfigurable user and space terminals for improved high-speed data communication links.

REFERENCES

[1] S. Liu, Z. Ma, J. Pei, Q. Jiao, L. Yang, W. Zhang, H. Li, Y. Li, Y. Zou, and X. Tan, "A review of anomalous refractive and reflective metasurfaces," *Nanotechnol. Precis. Eng.*, vol. 5, no. 2, Jun. 2022, Art. no. 025001.

[2] D. Sell, J. Yang, E. W. Wang, T. Phan, S. Doshay, and J. A. Fan, "Ultra-high-efficiency anomalous refraction with dielectric metasurfaces," *ACS Photon.*, vol. 5, no. 6, pp. 2402–2407, Jun. 2018.

[3] A. M. H. Wong and G. V. Eleftheriades, "Perfect anomalous reflection with a bipartite Huygens' metasurface," *Phys. Rev. X*, vol. 8, no. 1, Feb. 2018, Art. no. 011036.

[4] W. Guo, Y. Liu, and T. Han, "Ultra-broadband infrared metasurface absorber," *Opt. Exp.*, vol. 24, no. 18, 2016, Art. no. 20586.

[5] Q. Zhou, W. Ma, T. Wu, Y. Li, Q. Qiu, J. Duan, J. Li, L. Jiang, W. Zhou, Y. Gao, J. Huang, and Z. Huang, "Metasurface terahertz perfect absorber with strong multi-frequency selectivity," *ACS Omega*, vol. 7, no. 41, pp. 36712–36727, Oct. 2022.

[6] K. M. Kossifos, L. Petrou, G. Varnava, A. Pitilakis, O. Tsilipakos, F. Liu, P. Karousios, A. C. Tasolamprou, M. Seckel, D. Manessis, N. V. Kantartzis, D.-H. Kwon, M. A. Antoniades, and J. Georgiou, "Toward the realization of a programmable metasurface absorber enabled by custom integrated circuit technology," *IEEE Access*, vol. 8, pp. 92986–92998, 2020.

[7] X. Gao, W. L. Yang, H. F. Ma, Q. Cheng, X. H. Yu, and T. J. Cui, "A reconfigurable broadband polarization converter based on an active metasurface," *IEEE Trans. Antennas Propag.*, vol. 66, no. 11, pp. 6086–6095, Nov. 2018.

[8] M. K. Emara, T. Tomura, J. Hirokawa, and S. Gupta, "Metallo-dielectric millimeter-wave Huygens' quarter-wave and half-wave plates," *IEEE Trans. Antennas Propag.*, vol. 71, no. 8, pp. 6678–6687, Aug. 2023.

[9] Y.-T. Zhao, J.-J. Zhang, and B. Wu, "Low profile reflective polarization conversion metasurface with high frequency selectivity," *IEEE Trans. Antennas Propag.*, vol. 70, no. 11, pp. 10614–10622, Nov. 2022.

[10] J. Liao, C. Ji, L. Yuan, C. Huang, Y. Wang, J. Peng, and X. Luo, "Polarization-insensitive metasurface cloak for dynamic illusions with an electromagnetic transparent window," *ACS Appl. Mater. Interface*, vol. 15, no. 13, pp. 16953–16962, Apr. 2023.

[11] C. Wang, Y. Yang, Q. Liu, D. Liang, B. Zheng, H. Chen, Z. Xu, and H. Wang, "Multi-frequency metasurface carpet cloaks," *Opt. Exp.*, vol. 26, no. 11, p. 14123, May 2018.

[12] Y. Huang, M. Pu, F. Zhang, J. Luo, X. Li, X. Ma, and X. Luo, "Broadband functional metasurfaces: Achieving nonlinear phase generation toward achromatic surface cloaking and lensing," *Adv. Opt. Mater.*, vol. 7, no. 7, Apr. 2019, Art. no. 1801480.
[13] E. Martini and S. Maci, "Theory, analysis, and design of metasurfaces for smart radio environments," *Proc. IEEE*, vol. 110, no. 9, pp. 1227–1243, Sep. 2022.
[14] I. F. Akyildiz, A. Kak, and S. Nie, "6G and beyond: The future of wireless communications systems," *IEEE Access*, vol. 8, pp. 133995–134030, 2020.
[15] T. S. Rappaport, Y. Xing, O. Kanhere, S. Ju, A. Madanayake, S. Mandal, A. Alkhateeb, and G. C. Trichopoulos, "Wireless communications and applications above 100 GHz: Opportunities and challenges for 6G and beyond," *IEEE Access*, vol. 7, pp. 78729–78757, 2019.
[16] S. Gong, X. Lu, D. T. Hoang, D. Niyato, L. Shu, D. I. Kim, and Y.-C. Liang, "Toward smart wireless communications via intelligent reflecting surfaces: A contemporary survey," *IEEE Commun. Surveys Tuts.*, vol. 22, no. 4, pp. 2283–2314, 4th Quart., 2020.
[17] M. Di Renzo, A. Zappone, M. Debbah, M.-S. Alouini, C. Yuen, J. de Rosny, and S. Tretyakov, "Smart radio environments empowered by reconfigurable intelligent surfaces: How it works, state of research, and the road ahead," *IEEE J. Sel. Areas Commun.*, vol. 38, no. 11, pp. 2450–2525, Nov. 2020.
[18] B. Kress, *Field Guide to Digital Micro-Optics*. Bellingham, WA, USA: SPIE Press, 2014.
[19] G. Ding, K. Chen, X. Luo, G. Qian, J. Zhao, T. Jiang, and Y. Feng, "Direct routing of intensity-editable multi-beams by dual geometric phase interference in metasurface," *Nanophotonics*, vol. 9, no. 9, pp. 2977–2987, Jul. 2020.
[20] S. Pancharatnam, "Generalized theory of interference, and its applications," *Proc. Ind. Acad. Sci.*, vol. 44, no. 5, pp. 247–262, 1956.
[21] M. V. Berry, "The adiabatic phase and Pancharatnam's phase for polarized light," *J. Modern Opt.*, vol. 34, no. 11, pp. 1401–1407, Nov. 1987.
[22] J. S. Demetre, T. J. Smy, and S. Gupta, "Static metasurface reflectors with independent magnitude and phase control using coupled resonator configuration," *IEEE Trans. Antennas Propag.*, vol. 71, no. 4, pp. 3536–3545, Apr. 2023.
[23] G. Dong, J. Chen, J. Zhang, S. Zhu, A. Zhang, and X. Chen, "Multiple beams direction and power control using passive lossless metasurface by surface waves," *Opt. Commun.*, vol. 546, Nov. 2023, Art. no. 129843.
[24] J. C. Liang, L. Zhang, Z. W. Cheng, P. Zhang, and T. J. Cui, "Flexible beam manipulations by reconfigurable intelligent surface with independent control of amplitude and phase," *Frontiers Mater.*, vol. 9, Jul. 2022, Art. no. 946163.
[25] S. Han, S. Kim, S. Kim, T. Low, V. W. Brar, and M. S. Jang, "Complete complex amplitude modulation with electronically tunable graphene plasmonic metamolecules," *ACS Nano*, vol. 14, no. 1, pp. 1166–1175, Jan. 2020.
[26] R. Phon, M. Lee, C. Lor, and S. Lim, "Multifunctional reflective metasurface to independently and simultaneously control amplitude and phase with frequency tunability," *Adv. Opt. Mater.*, vol. 11, no. 14, Jul. 2023, Art. no. 2202943.
[27] B. Zheng, H. Ren, S. An, H. Tang, H. Li, M. Haerinia, Y. Dong, C. Fowler, and H. Zhang, "Tunable metasurface with dynamic amplitude and phase control," *IEEE Access*, vol. 9, pp. 104522–104529, 2021.
[28] K. MacDonell, D. Kundu, C. Andersen, L. M. Rufail, and S. Gupta, "A mechatronic shape-shifting reflector system with true independent reflection magnitude and phase control for dynamic beamforming," *IEEE Trans. Antennas Propag.*, 2023. [Online]. Available: https://www.techrxiv.org/articles/preprint/A_Mechatronic_Shape-shifting_Reflector_System_with_True_Independent_Reflection_Magnitude_and_Phase_Control_for_Dynamic_Beamforming/23735958
[29] X. Yang, S. Xu, F. Yang, M. Li, Y. Hou, S. Jiang, and L. Liu, "A broadband high-efficiency reconfigurable reflectarray antenna using mechanically rotational elements," *IEEE Trans. Antennas Propag.*, vol. 65, no. 8, pp. 3959–3966, Aug. 2017.
[30] Z. Cao, Y. Li, Z. Zhang, and M. F. Iskander, "Single motor-controlled mechanically reconfigurable reflectarray," *IEEE Trans. Antennas Propag.*, vol. 71, no. 1, pp. 190–199, Jan. 2023.
[31] H. L. Wang, Y. K. Zhang, T. Y. Zhang, H. F. Ma, and T. J. Cui, "Broadband and programmable amplitude-phase-joint-coding information metasurface," *ACS Appl. Mater. Interface*, vol. 14, no. 25, pp. 29431–29440, Jun. 2022.
[32] Q. Hu, J. Yang, W. Yang, K. Qu, X. Ge, H. Tang, J. Zhao, T. Jiang, K. Chen, and Y. Feng, "Joint amplitude-phase metasurface for polarization-selective dynamic wavefront manipulation and broadband absorption," *Adv. Mater. Technol.*, vol. 8, no. 15, Aug. 2023, Art. no. 2300111.
[33] M. K. Emara, D. Kundu, K. MacDonell, L. M. Rufail, and S. Gupta, "Coupled resonator-based metasurface reflector with enhanced magnitude and phase coverage," *IEEE Trans. Antennas Propag.*, 2023. [Online]. Available: https://www.techrxiv.org/articles/preprint/Coupled_Resonator-Based_Metasurface_Reflector_with_Enhanced_Magnitude_and_Phase_Coverage/22635577
[34] C. L. Holloway and E. F. Kuester, "Generalized sheet transition conditions for a metascreen—A fishnet metasurface," *IEEE Trans. Antennas Propag.*, vol. 66, no. 5, pp. 2414–2427, May 2018.
[35] B. E. Saleh and M. C. Teich, *Fundamentals of Photonics*. Hoboken, NJ, USA: Wiley, 2019.
[36] K. Achouri, M. A. Salem, and C. Caloz, "General metasurface synthesis based on susceptibility tensors," *IEEE Trans. Antennas Propag.*, vol. 63, no. 7, pp. 2977–2991, Jul. 2015.
[37] *Skyworks SMV2019 Series*. Accessed: Aug. 26, 2023. [Online]. Available: https://www.skyworksinc.com/Products/Diodes/SMV2019-series
[38] *Skyworks SMP1302 Series*. Accessed: Aug. 26, 2023. [Online]. Available: https://www.skyworksinc.com/en/products/diodes/smp1302-series
[39] B. Liu, Y. He, S. Wong, and Y. Li, "Multifunctional vortex beam generation by a dynamic reflective metasurface," *Adv. Opt. Mater.*, vol. 9, no. 4, Feb. 2021, Art. no. 2001689.
[40] Y. Saifullah, Q. Chen, G.-M. Yang, A. B. Waqas, and F. Xu, "Dual-band multi-bit programmable reflective metasurface unit cell: Design and experiment," *Opt. Exp.*, vol. 29, no. 2, p. 2658, Jan. 2021.
[41] X. Song, X. Bai, and W. Zhu, "Reconfigurable metasurface for nearly full-range and continuous modulation of reflection, transmission, and absorption," *ACS Appl. Electron. Mater.*, vol. 4, no. 3, pp. 1225–1231, Mar. 2022.
[42] C. Balanis, *Antenna Theory: Analysis and Design*. Hoboken, NJ, USA: Wiley, 2015.
[43] K. Zheng, K. Xu, S. Chen, T. Zhou, X. Pan, C. Zhang, and X. Yu, "One-bit wideband reconfigurable reflectarray with stable beam-scanning gain for X-band application," *Microw. Opt. Technol. Lett.*, vol. 65, no. 8, pp. 2323–2330, Aug. 2023.
[44] L. M. Rufail, M. K. Emara, A. Z. Ashoor, and S. Gupta, "Metasurface reflector with independent polarizations control using a supercell concept," in *Proc. IEEE Int. Symp. Antennas Propag. USNC-URSI Radio Sci. Meeting (AP-S/URSI)*, Jul. 2022, pp. 1880–1881.
[45] M. K. Emara, L. M. Rufail, and S. Gupta, "Coupled resonator metasurface supercell for independent control of orthogonal polarizations with enhanced complex reflectance," in *Proc. URSI General Assem. Sci. Symp.*, 2023, p. 1.

MOHAMED K. EMARA (Member, IEEE) received the B.Eng. degree in aerospace engineering and the M.A.Sc. and Ph.D. degrees in electrical and computer engineering from Carleton University, Ottawa, ON, Canada, in 2016, 2018, and 2023 respectively. His M.A.Sc. thesis focused on dispersive electromagnetic structures for surface wave control on antenna ground planes and guided wave control in half-mode substrate integrated waveguides. His Ph.D. thesis explored analog beamforming techniques using leaky-wave antennas, passive metasurface transmitters, and passive/active metasurface reflectors.

He is currently a Senior Antenna and RF Designer with Tallysman Wireless Inc., Ottawa, where he develops antenna solutions for global navigation satellite systems (GNSS). He was a recipient of the Undergraduate Senate Medal for Outstanding Academic Achievement, in 2016, the Ontario Graduate Scholarship, from 2016 to 2017 and from 2020 to 2021, the Student Paper Competition Winner from the 2018 International Symposium on Antenna Technology and Applied Electromagnetics, the Natural Sciences and Engineering Research Council (NSERC) Alexander Graham Bell Canada Graduate Scholarship, from 2020 to 2023, and the Honorable Mention in the Student Paper Competition from the 2020 IEEE Antennas and Propagation Symposium. He also received the Graduate Senate Medal for Outstanding Academic Achievement for the Ph.D. thesis, in 2023.

DEBIDAS KUNDU (Member, IEEE) received the B.Tech. degree in electronics and communication engineering from the West Bengal University of Technology, India, in 2011, the M.E. degree in electronics and telecommunication engineering from IIEST, Shibpur, India, in 2013, and the Ph.D. degree from the Department of Electronics and Electrical Communication Engineering, Indian Institute of Technology Kharagpur, India, in 2018.

From 2018 to 2019, he was with BITS Pilani K. K. Birla Goa Campus as a Visiting Faculty. From 2019 to 2023, he was a DST-INSPIRE Faculty Member with the Department of Electronics and Communication Engineering, Indian Institute of Technology Roorkee. From 2022 to 2023, he was a Visiting Researcher (Postdoctoral Researcher) with Carleton University, Canada. He is currently an Assistant Professor with the Department of Electronics and Communication Engineering, Indraprastha Institute of Information Technology Delhi. His current research interests include frequency selective surface and metasurface, analytical techniques, scattering and polarization control of the electromagnetic wave, reflectarray, and reconfigurable intelligent surface. He was a recipient of the 2018 INSPIRE Faculty Award from the Department of Science and Technology, Government of India, and the 2020 and 2023 Young Scientist Awards from the URSI Regional Conference on Radio Science and the URSI General Assembly and Scientific Symposium, respectively.

KEIGAN MACDONELL (Member, IEEE) received the B.Eng. degree in aeronautical engineering and the M.A.Sc. degree in electronics from Carleton University, Ottawa, ON, Canada, in 2021 and 2023, respectively. He is currently a Graduate Student with the Metamaterials and Antennas Research Squad, Carleton University, where he continues to conduct research into metasurface design.

LEANDRO M. RUFAIL received the bachelor's degree in electrical engineering from Universidad Católica de Córdoba, Córdoba, Argentina, in 2000, and the M.A.Sc. and Ph.D. degrees from École Polytechnique de Montréal, Canada, in 2012 and 2020 respectively.

In 2020, he joined Carleton University, where he focused on research of smart metamaterial reflectors. His research interests include low-profile antennas for aviation applications and microwave techniques for non-destructive evaluation of aircraft materials. He was a recipient of the NSERC Industrial Innovation Scholarships Program, where he was involved in close collaboration with Bombardier Aerospace Inc.

SHULABH GUPTA (Senior Member, IEEE) was born in Etah, India, in 1982. He received the B.Tech. degree in electronic engineering from IIT (Indian School of Mines) at Dhanbad, Dhanbad, India, in 2004, the M.S. degree in telecommunications from the Institut National de la Recherche Scientifique Energie Materiaux Telecommunications Research Center, Université du Québec, Montreal, QC, Canada, in 2006, and the Ph.D. degree in electrical engineering from the École Polytechnique de Montréal, Montreal, in 2012.

From 2009 to 2010, he was a Visiting Research Fellow with the Tokyo Institute of Technology, Tokyo, Japan, followed by a Postdoctoral Fellow with the University of Colorado at Boulder, Boulder, CO, USA, in 2012. He was also a Postdoctoral Fellow with The University of Hong Kong, Hong Kong, from 2012 to 2014, and École Polytechnique de Montréal, from 2014 to 2016. He is currently an Associate Professor with the Department of Electronics, Carleton University, Ottawa, ON, Canada. He is also a Licensed Professional Engineer in Ontario. He was a recipient of the Young Scientist Award from the International Symposium on Electromagnetic Theory Ottawa, in 2007, the International Union of Radio Science-General Assembly, Chicago, in 2008, and ISAP Jeju, in 2011. His thesis received the Best Doctoral Dissertation Award from École Polytechnique de Montréal, in 2012, the Prix d'excellence de l'Association des doyens des etudes supérieures au Québec, in 2013, and the Academic Gold Medal of the Governor General of Canada. He is currently an Associate Editor of IEEE Antennas and Wireless Propagation Letters.